*Progress In Electromagnetics Research B, Vol. 103, 19–36, 2023*

# 3-D Electrical Impedance Imaging of Lung Injury

**Ming Ma[1], Zepeng Hao[2], Qi Wang[2], Xiuyan Li[2], Xiaojie Duan[2], Jianming Wang[3], and Hui Feng[4, *]**

**Abstract**—Pulmonary edema assessment is a key factor in monitoring and guiding the treatment of critically ill patients. To date, the methods available at the bedside to estimate the physiological correlation of pulmonary edema and extravascular pulmonary fluid are often unreliable or require invasive measurements. The aim of this article is to develop an imaging method of reliably assessing pulmonary edema by utilizing functional electrical impedance tomography. In this article, the Split-Bregman algorithm is used to solve the Total Variation (TV) minimization problem in EIT image reconstruction. A thorax model is constructed according to CT images of rats. Through simulation and experiment, the proposed method improves the quality of reconstructed image significantly compared with existing methods. A pulmonary edema experiment in rats is also carried out. The development of pulmonary edema is analyzed numerically through EIT images.

## 1. INTRODUCTION

Assessment of pulmonary edema in patients is a key factor in guiding treatment, especially in critically ill patients. Pulmonary edema [1] is an increase in water content in the lungs caused by the disturbance of fluid exchange between blood vessels and tissues in lungs [2]. This disease can seriously affect the respiratory function, and it is a common clinical cause of acute respiratory failure [3]. Studies have shown that pulmonary edema develops rapidly and can lead to serious and even life-threatening complications if not diagnosed in time [4, 5]. Therefore, a real-time and safe monitoring tool is needed for early diagnosis of pulmonary edema patients.

In recent years, medical imaging techniques such as computed tomography (CT) and magnetic resonance imaging (MRI) have been used to obtain high-resolution anatomical images of the thorax, allowing regional information to be obtained about injured lungs [6, 7]. However, the traditional medical imaging methods cannot provide real-time monitoring of the human body. As a functional imaging technology, electrical impedance tomography (EIT) can capture the dynamic characteristics of pulmonary edema in real time for analyzing the process of pulmonary edema [8, 9]. EIT is a novel imaging method that is nonionizing and noninvasive, making it a very attractive tool for continuous bedside imaging [10–12]. Given its ability to assess regional characteristics of lung structure, it can be considered an ideal tool for monitoring heterogeneous lung in acute pulmonary edema.

EIT imaging is an inverse problem [13]. Due to lack of measured data and ill-conditioned sensitivity matrix, the spatial resolution of reconstructed images is low, and measurement noise often produces image artifacts [14]. Many direct and iterative methods are used in EIT image reconstruction [15]. Since longitudinal changes in lung structure could not be analyzed by 2D EIT, 3D EIT is used for the analysis in this article. Traditional algorithms optimize computations by penalizing the L2 norm of the solution, such as Tikhonov regularization and Laplacian regularization [16, 17]. These L2-norm

*Received 6 June 2023, Accepted 6 September 2023, Scheduled 20 September 2023*
* Corresponding author: Hui Feng (fenghui007@njmu.edu.cn).
[1] School of Life Science, TianGong University, Tianjin 300382, China. [2] School of Electronic and Information Engineering, TianGong University, Tianjin 300382, China. [3] School of Computer Science and Technology, TianGong University, Tianjin 300382, China. [4] Department of Rehabilitation Medicine, The Affiliated Jiangning Hospital of Nanjing Medical University, China.

regularization algorithms smooth the edge features of an electrical impedance distribution and always cause distortion [18, 19].

With the complexity of the model and medium distribution, stronger L1-norm regularization is required. The Total Variation (TV) method is an L1-norm regularization that can be solved by methods such as Primal-Dual Interior Point Method (PDIPM), Linearized Alternating Direction Method of Multipliers (LADMM), and Split-Bregman [20–22]. TV regularization has received much attention, especially in electrical tomography in recent years [23, 24]. The TV method is primarily applied in the fields of image denoising and image restoration, focusing on differences in the two-dimensional spatial dimension [25]. In the context of EIT, the two-dimensional TV method has been widely used for image reconstruction and imaging problems [26]. With further research, it becomes evident that 3D-TV has more pronounced advantages over traditional TV in EIT imaging. Since EIT is inherently a volume-based imaging technique, the 3D-TV method can better consider the distribution and variations of conductivity in the entire three-dimensional space. By incorporating the 3D-TV method, EIT imaging can more comprehensively describe the conductivity distribution in the target region, leading to improved accuracy and stability in imaging.

In this article, a realistic 3D thorax model is constructed based on the anatomical structure of the rat thorax. To better observe the process of pulmonary edema in rats, Split-Bregman algorithm is used to solve the isotropic 3D-TV minimization problem of EIT image reconstruction. According to simulation and experiment results, our method has significantly improved the quality of reconstructed images compared with traditional conjugate gradient (CG) and TV algorithms [22, 27]. The development of pulmonary edema in rats can be continuously monitored according to the EIT technique.

The article is organized as follows. In Section 2, the basic mathematical model based on TV regularization for EIT is briefly described. Section 3 introduces the 3D-TV regularization with its solution based on the Split-Bregman iteration. In Section 4, the establishment of a 3D chest model for a rat was presented, and the forward problem of EIT was addressed. In Section 5, a numerical experiment of 3D EIT lung imaging of rats is designed, and a series of parameters for 3D-TV method are studied and selected. In Section 6, 3D reconstruction and analysis of the entire process for pulmonary edema in rats are performed. Finally, the conclusions are drawn in Section 7.

## 2. BASICS OF EIT RECONSTRUCTION

The relationship between the variations of electrical conductivity distribution $\sigma$ within the region of EIT reconstruction and the measured boundary voltage difference $V$ can be expressed as follows:

$$V = F(\sigma) + e \tag{1}$$

where $F$ is the nonlinear forward operator, and $e$ is the measurement error. To simplify the measurement process and mathematical modeling, the linearized EIT model assumes that the measurements of boundary voltage difference $V$ can be approximated by the product of the sensitivity matrix (J) and the perturbation of the conductivity distribution ($\sigma$) at a reference or baseline state. In practical scenarios, (1) can be linearized as

$$V = J\sigma + e \tag{2}$$

In this article, a chest model with a homogeneous distribution of conductivity is used as a reference. The inverse problem in EIT image reconstruction involves the process of deriving the conductivity distribution from measured voltage data [28]. For this process, it can be formulated as:

$$\sigma^* = \arg\min_{\sigma} ||J\sigma - V||_2^2 + \lambda\varphi(\sigma) \tag{3}$$

To incorporate TV regularization into this optimization problem, a collection of transforms or operators on $\sigma$ is considered. The non-separable penalty function is specified as:

$$\varphi(\sigma) = \sum_i ||D_i\sigma||_2 \tag{4}$$

where $\sum_i$ is taken over all voxels. We define $N$ as the total number of discretized voxels. For any $i$, $D_i$ in Equation (4) is a 3-by-N matrix such that the three entries of $D_i\sigma$ represent $D_i \triangleq (D_i^{(1)}; D_i^{(2)}; D_i^{(3)})$,

where $D_i^{(1)}$, $D_i^{(2)}$, and $D_i^{(3)}$ are discrete differences along the $x$, $y$, and $z$ directions. As such, $D^{(1)}$, $D^{(2)}$, and $D^{(3)}$ contain, respectively, the first, second, and third rows of $D_i$ for all $i$. In the rest of this paper, we let $||\cdot|| = ||\cdot||_2$.

## 3. 3D-TV ALGORITHM BASED ON SPLIT-BREGMAN ITERATION

Solving Equation (3) is not straightforward, so a variable splitting algorithm is introduced to solve the equation [29]. We formulate the regularized matrix recovery scheme as a constrained minimization problem using variable splitting:

$$\sigma^* = \arg\min_{\sigma,S} ||J\sigma - V||^2 + \lambda \sum_i ||S_i|| \text{ such that } S_i = D_i\sigma; \tag{5}$$

Here, $S_i$ is an auxiliary variable, which is also determined during the optimization process. The fundamental principle behind the Split-Bregman method is that the constrained optimization problem is simpler to solve than its unconstrained version, specified by Equation (3). We solve Equation (5) using the penalty method, where we minimize

$$\mathcal{D}_\beta(\sigma, S_i) = ||J\sigma - V||^2 + \lambda \sum_i ||S_i|| + \frac{\beta}{2} \sum_i ||D_i\sigma - S_i||^2 \tag{6}$$

The third term of (6) is the penalties introduced to enforce the constraints $S_i = D_i\sigma$. The solution of problem (6) tends to that of (5), when $\beta \to \infty$. The selection of $\lambda$ plays a crucial role in balancing data fitting and structural constraints, and it has a significant impact on the solution of optimization problems. It influences the sparsity of the final solution and the level of model simplification.

We solve (6) using a two-step alternating minimization scheme, assuming that the remaining variables are known in order to solve for one variable of interest:

$$\sigma_{n+1} = \arg\min_{\sigma} \|J\sigma - V\|^2 + \frac{\beta}{2} \sum_i \|D_i\sigma - S_{i,n}\|^2 \tag{7}$$

$$S_{i,n+1} = \arg\min_{\{S_i\}} \sum_i \|D_i\sigma_{n+1} - S_i\|^2 + \frac{2\lambda}{\beta} \sum_i \|S_i\| \tag{8}$$

The first sub-problem (7) is quadratic and hence can be solved analytically as:

$$\sigma_{n+1} = \left(J^TJ + \frac{\beta}{2}\sum_i D_i^TD_i\right)^{-1}\left(J^TV + \frac{\beta}{2}\sum_i S_i\right) = \mathcal{T}(S_i) \tag{9}$$

where the operator $Q_i$ is defined as $Q_i(\sigma) = D_i\sigma$. Then Equation (7) is solved using a few conjugate gradient steps.

The solution to the second sub-problem (8) requires the joint processing of all the terms $Q_i(\sigma_{n+1})$, so that the magnitude, specified by $\sum_i \|Q_i(\sigma_{n+1})\|^2$, is reduced:

$$S_{i,n+1} = \frac{D_i(\sigma_{n+1})}{\sum_i \|D_i(\sigma_{n+1})\|^2} \cdot \left(\sum_i \|D_i(\sigma_{n+1})\|^2 - \frac{\lambda}{\beta}\right)_+ = \kappa_{\lambda/\beta}(\sigma_{n+1}) \tag{10}$$

This approach is termed as multidimensional shrinkage of $Q_i(\sigma_{n+1})$ [30, 31]. Note that Table 1 involves two loops in the algorithm. The parameter $\beta$ is incremented in the outer loop, while the minimization of $\mathcal{D}_\beta(\sigma S_i)$ is performed in the inner loop. We terminate the inner iteration when the stopping criterion, specified by

$$d_n = \left|\frac{\mathcal{D}_{\beta_p}(\sigma_n) - \mathcal{D}_{\beta_p}(\sigma_{n-1})}{\mathcal{D}_{\beta_p}(\sigma_n)}\right| < TOLERANCE \tag{11}$$

is satisfied.

**Table 1.** The procedure of the 3D-TV algorithm for EIT reconstruction is summarized.

| Algorithm 1 3D-TV Algorithm for EIT Reconstruction |
|---|
| Input: $V$, $J$, $\sigma_0$, TOLERANCE |
| Output: $\sigma_{n+1}$ |
| 1: Initialize $p = 0$; $\beta_0 > 0$; $S_i = 0$; |
| 2: while $S_i \neq D_i\sigma$ do |
| 3: while $d_n >$ TOLERANCE do |
| 4: Solve (9) for $\sigma_{n+1}$ according to equation (7) |
| 5: Solve (10) for $S_{i,n+1}$ according to equation (8) |
| 6: $n = n + 1$; |
| 7: end while |
| 8: $\beta_{p+1} = \beta_p *$ INC_FACTOR; $p = p + 1$; |
| 9: end while |

## 4. 3D MODEL BUILDING

CT scanning sequences of rat lungs were acquired using a CT scanner (Siemens SOMATOM Force dual source CT) (Figure 1), providing valuable information about the internal structure of the rats. A three-dimensional model of the rat thorax was developed based on these CT data.

Figure 2 illustrates the specific workflow for constructing the 3D thoracic model of the rat. The model has been simplified to include only the lungs within the thorax cavity. Lung and thorax contours are extracted based on the Maximum Interclass Variance algorithm [32] and superimposed to obtain a preliminary model of thorax. Firstly, the contours of the chest and lungs are extracted using the algorithm. Subsequently, the contours are overlaid to construct a preliminary chest model of the rat's thoracic cavity and lungs in Mimics (Mimics Medical 21.0). SolidWorks (SolidWorks 2020) can be employed to perform model smoothing, thereby enabling the acquisition of stable solutions in forward problems. Finally, the thoracic model and lung model are imported into COMSOL Multiphysics (COMSOL Multiphysics 5.4) to solve the forward problem of EIT.

The 3D rat thorax model is established in Figure 3. We distributed a single ring of 16 electrodes evenly around the rat thorax. Experimental determination of the electrical conductivity for biological tissues was performed. The electrical conductivities for rat pulmonary and non-pulmonary tissues are set to 0.12 S/m and 0.48 S/m, respectively.

The Finite Element Method (FEM) was used to solve the forward problem. The resulting mesh of the 3D thorax model was created by COMSOL and consisted of 45917 first-order tetrahedral domain elements (Figure 4).

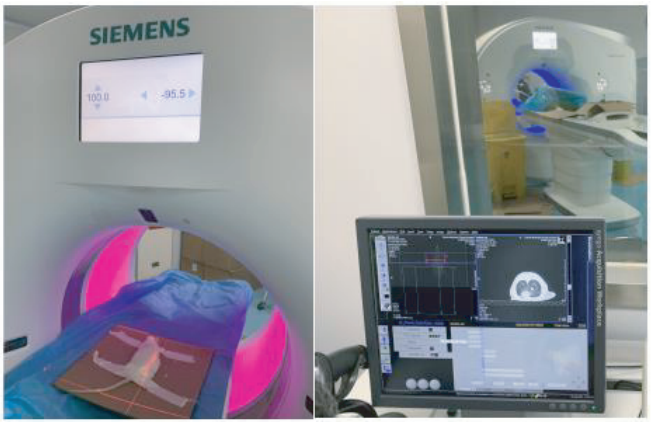


**Figure 1.** CT scans of rat.

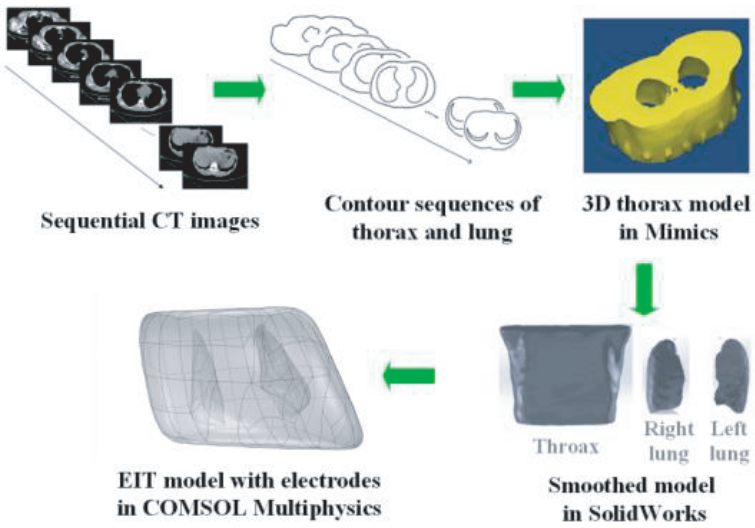


**Figure 2.** Steps for constructing a three-dimensional rat chest model.

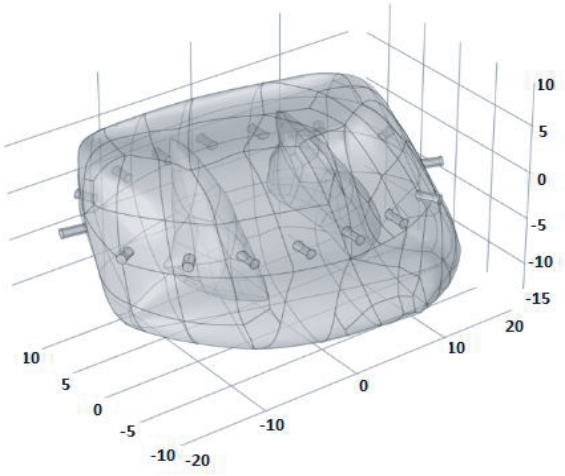


**Figure 3.** 3D rat thorax model.

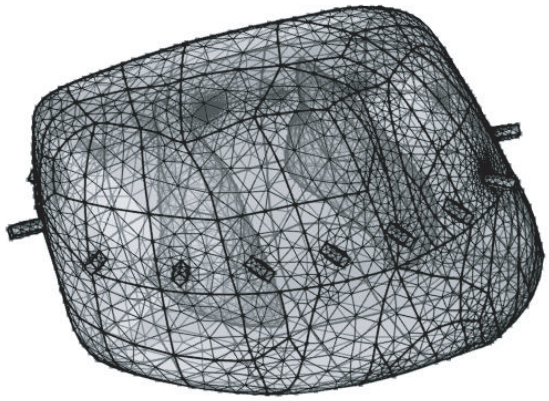

**Figure 4.** FEM of 3D thorax model.

Based on the three-dimensional effect of the electric field, it is possible to reconstruct images both within and outside a measurement plane from the measured results on an electrode plane. Figure 5 shows the current density images of finite element simulations with complex conductivity distributions at four excitation locations. It can be seen that the current is distributed throughout the 3D lung, so that 3D lung information can be extracted from EIT measurements using a single-ring electrode. In the plane where the electrodes are located, the current density is high. The current density decreases with increasing distance from the electrode plane.

To obtain the 3D reconstruction result, the images could be reconstructed onto multiple voxel layers perpendicular to the $z$-axis with the measurements from the single-ring electrode plane [33]. Considering the memory limits and speed requirements, there are 45 reconstruction layers in the 3D reconstructed image, and each layer has a resolution of $32 \times 32$. The reconstruction layer separation is 0.5 mm. The 3D mesh for the inverse problem is shown in Figure 6.

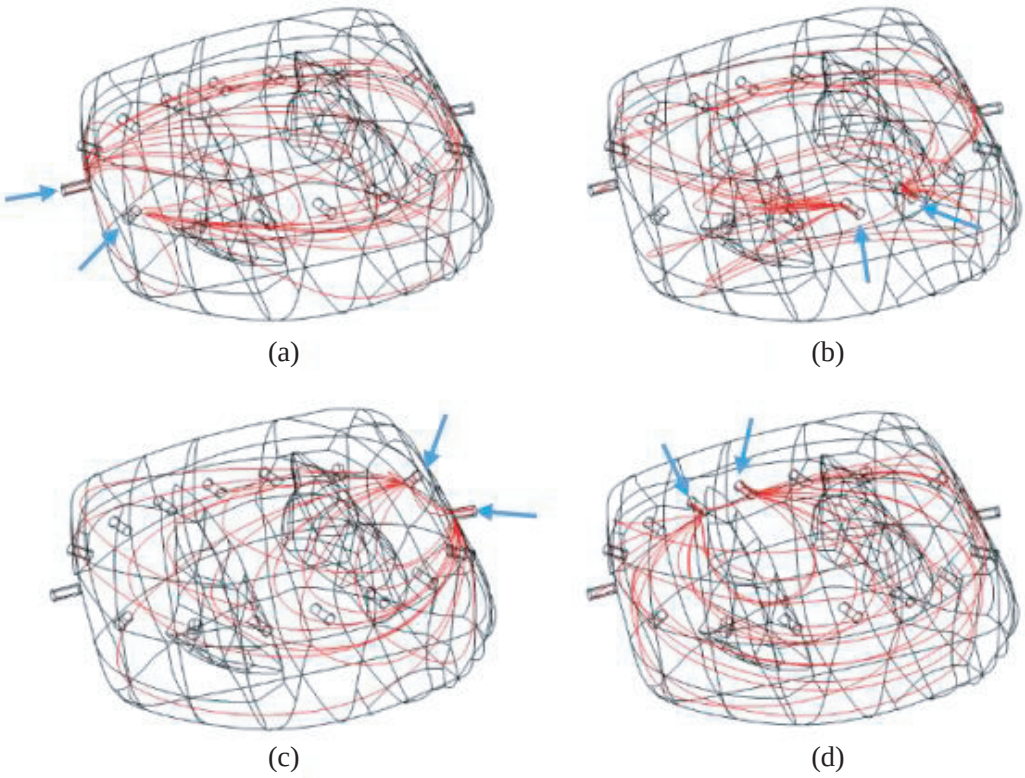


**Figure 5.** Current density distribution in a 3D model of the rat thorax: (a) excitation electrode on the left side of the thorax; (b) excitation electrode in the front of the thorax; (c) excitation electrode on the right side of the thorax; (d) excitation electrode in the back of the thorax.

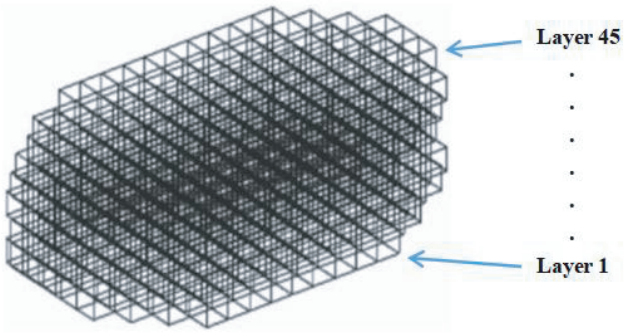


**Figure 6.** Voxel mesh for solving inverse problem.

## 5. NUMERICAL SIMULATION AND RECONSTRUCTION

This section presents the parameter selection strategy and methodology of the 3D-TV algorithm based on the 3D thoracic model of the rat. By conducting imaging of the rat lungs, a thorough analysis of the reconstruction results obtained through this approach is performed.

### 5.1. Selection of Parameters for the 3D-TV Algorithm

This section focuses on the parameter selection issue of the 3D-TV algorithm through numerical simulation-based investigations.

*5.1.1. Iteration Number*

In this section, a comparison was made among the CG algorithm, traditional TV regularization algorithm, and 3D-TV regularization algorithm in terms of their impact on the quality of lung reconstruction images at different iteration steps. The relative error (RE) and Residual were utilized to assess the image reconstruction quality. The $RE$ is used to measure the difference between the reconstructed image and the original image, while the Residual is used to quantify the difference between the reconstructed image and the measured data.

$$RE = \frac{\left\| \sum_{i=1}^{N} (\sigma_i - \sigma_i^*) \right\|_2}{\sum_{i=1}^{N} \sigma_i^*} \tag{12}$$

$$Residual = ||V - J\sigma||_2^2 \tag{13}$$

where $\sigma_i$ is the reconstructed conductivity of the $i$th voxel, $\sigma_i^*$ the truth value, and $N$ the number of voxels.

In order to evaluate the accuracy of the obtained results, we performed quantitative calculations of the $RE$ values and Residuals defined at each iteration step. The $RE$ and Residual curves are provided in Figure 7 to compare the convergence rates of the three methods. The curves in Figure 7 demonstrate that the 3D-TV method converges much faster than the other two methods. Considering both accuracy and efficiency factors, we empirically determined the number of iteration steps for the 3D-TV method to be 50.

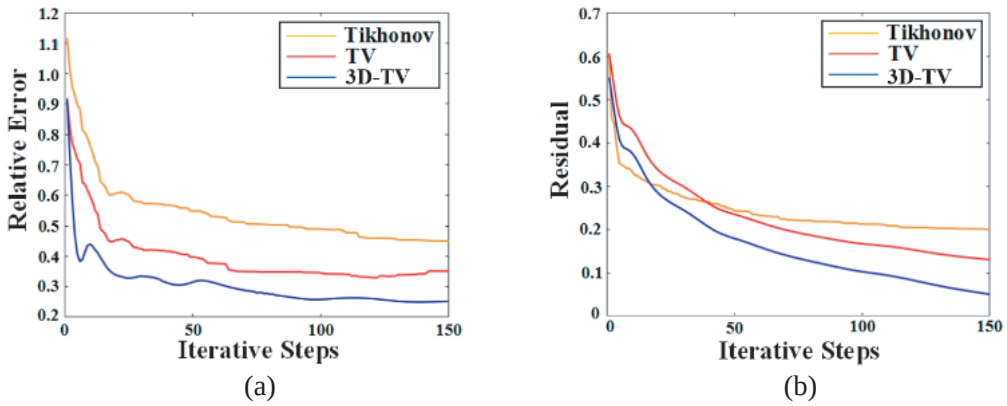


**Figure 7.** Comparing convergence rates of reconstruction algorithms at end-inspiration status.

*5.1.2. Regularization Parameter*

The weight of the regularization parameter $\lambda$ is crucial. When the number of iterations in this article is selected as 50, the influence of the regularization parameter of the 3D-TV method on the $RE$ value of the reconstructed image is shown in Figure 8.

According to Figure 8, it can be seen that with the constant change of the regularization parameter, the $RE$ value of the reconstructed image gradually decreases and reaches the minimum value when the regularization parameter is 1e-16. The $RE$ value then increases slightly and remains unchanged. Therefore, the regularization parameter of the 3D-TV method is chosen to be 1e-16 during the EIT reconstruction.

## 5.2. 2D and 3D Reconstruction Results of Rat Lung

EIT images were generated for rat lungs using different algorithms. Lung areas were divided into 31 horizontal layers (from the 9th to the 39th layer of the entire model). Figure 9 displays eight image

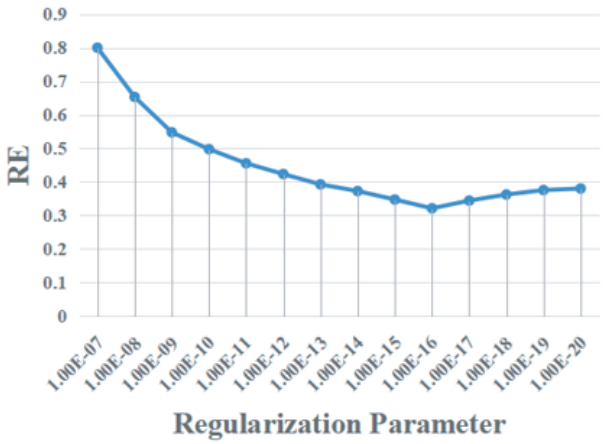


**Figure 8.** The influence of the choice of regularization parameters on $RE$.

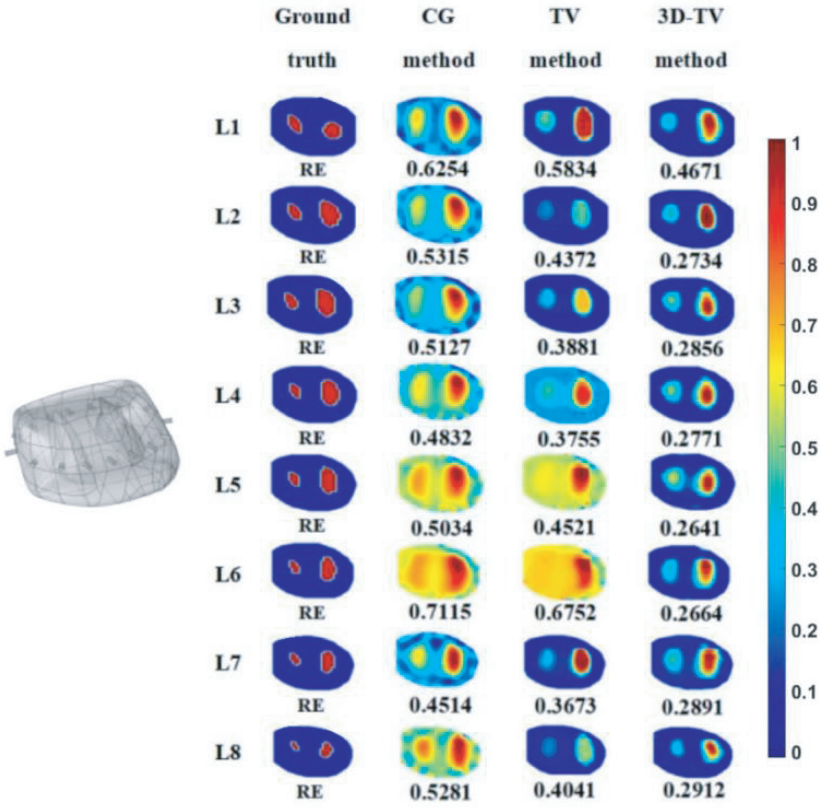


**Figure 9.** 2-D lung images reconstructed using three algorithms.

slices of rat lungs reconstructed using different algorithms. The images are presented in order from bottom to top according to the simulation model, which includes the lung region. It is evident that all three algorithms effectively capture changes in the lung area in 3D dimensions. While both TV and 3D-TV methods demonstrate edge-preserving effects, the 3D-TV method exhibits superior lung volume distinction.

As shown in Figure 10, the 3D reconstruction of rat lung is achieved by the CG algorithm, traditional TV algorithm, and 3D-TV algorithm, respectively. We explored the internal structure of the thoracic cavity in-depth by providing coronal and sagittal slices of the three-dimensional reconstructed

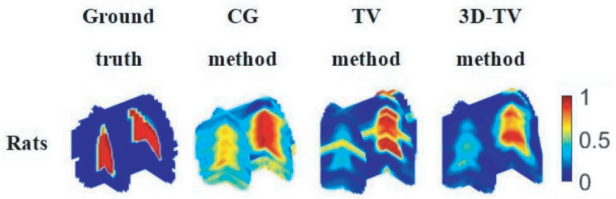


**Figure 10.** 3D lung of rat reconstruction results based on simulation data.

images. According to the reconstruction results in Figure 10, 3D lung volumes could be shown. The reconstruction results of the CG method and traditional TV regularization method have artifacts in the entire lung area or near the electrodes, while the reconstruction results of the 3D-TV method, as compared to CG and traditional TV methods, have shown improved edge-preserving performance in the inversion results.

### 5.3. Analysis of 3D EIT Reconstruction Results

In this section, the analysis of three-dimensional EIT reconstruction results was conducted using lung volume, Correlation Coefficient (CC) and Structural Similarity Index Measurement (SSIM).

#### *5.3.1. Lung Volume*

One of the main advantages of 3D EIT is its potential to capture regional lung activity inhomogeneities within a volume. To analyze lung volumes from 3D EIT data, we conducted a study on rat lung volume using the Lung Region Ratio (LRR). Based on 3D reconstructed images, the $LRR$ values for rat lung is calculated according to (14) and given in Table 2.

$$LRR = \frac{VA}{TA + VA} \tag{14}$$

Ventilated Area (VA) refers to the area of the lung that actively participates in ventilation. It represents the portion of the lung that is involved in gas exchange during respiration. Thoracic Area (TA) refers to the area outside the lung, which includes the rib cage and other structures of the thoracic cavity. It represents the region surrounding the lung within the chest cavity. The $LRR$ values from reconstructed images are compared to those from real images by calculating the errors.

$$error_{LRR} = LRR_{recons} - LRR_{real} \tag{15}$$

$error_{LRR}$ represents the discrepancy or error between the $LRR_{recons}$ obtained from the reconstruction results and the true $LRR_{real}$ obtained from the simulated model constructed through CT scanning in Section 4. It quantifies the difference between the reconstructed $LRR$ and the ground truth $LRR$.

The $LRR$ can provide information about the distribution of ventilation throughout the entire thoracic cavity, allowing for the assessment of lung ventilation uniformity or abnormalities. From Table 2, the $LRR$ parameters estimated from the rat lung reconstruction results indicate that the 3D-TV method is most suitable for calculating lung ventilation.

**Table 2.** Comparison of LRR based on simulation data of rat.

| | **Real** | **CG** | **TV** | **3D-TV** |
|---|---|---|---|---|
| LRR | 0.1364 | 0.1978 (0.0614) | 0.1692 (0.0328) | 0.1395 (0.0031) |

*5.3.2. Correlation Coefficient*

The Correlation Coefficient (CC) quantifies the correlation between the true model and the reconstructed model [15]:

$$CC = \frac{Cov(\sigma_{true}, \hat{\sigma})}{Std\,(\sigma_{true}) * Std(\hat{\sigma})} \tag{16}$$

$CC$ in the formula is computed by calculating the covariance ($Cov$) between the true model $\sigma_{true}$ and the estimated model $\hat{\sigma}$. Here, $Cov$ is used to quantify the correlation between the true model and the reconstructed model. $Std\,(\sigma_{true})$ and $Std(\hat{\sigma})$ respectively represent the standard deviations of the true and reconstructed models, which are used for normalizing the covariance. The range of the $CC$ is between 0 and 1. When $CC$ is closer to 1, the reconstructed results and the true model has higher similarity. That means the reconstruction has greater accuracy.

*5.3.3. Structural Similarity Index Measurement*

The Structural Similarity Index Measurement (SSIM) is used to calculate the similarity between the true model and the reconstructed image [33]:

$$SSIM = \frac{(2\mu_x\mu_y + C_1)\,(2\sigma_{xy} + C_2)}{\left(\mu_x^2+\mu_y^2 + C_1\right)\left(\sigma_x^2+\sigma_y^2 + C_2\right)} \tag{17}$$

where $\mu_x$ and $\mu_y$ denote the mean values of $x$ and $y$. $\sigma_x$ and $\sigma_y$ are standard deviations of images $x$ and $y$. $\sigma_{xy}$ is the covariance of images $x$ and $y$. $C_1$ and $C_2$ are constants, which are used to prevent the divisor being 0. $x$ is the ground truth conductivity, $y$ is the estimated conductivity. A larger $SSIM$ value indicates a higher image similarity.

Figure 11 displays the calculated values of $RE$, $CC$, and $SSIM$ based on the 3D reconstructed images of the rat lungs.

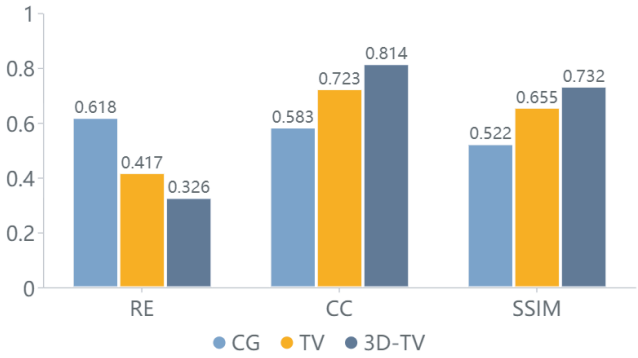


**Figure 11.** The $RE$, $CC$ and $SSIM$ values based on 3D reconstructed images for rat lung.

From Figure 11, $RE$, $CC$ and $SSIM$ values of the rat lungs under different reconstruction algorithms could be compared. Besides better visual quality of the images, the 3D-TV method has the largest $CC$ and $SSIM$ values, which are closer to 1, compared to the CG and traditional TV methods. This shows that the 3D-TV regularized reconstruction result is significantly improved in reconstruction quality.

## 6. EXPERIMENTAL RESULTS

### 6.1. Animals and Groups

The animal experiments were conducted at the Institute of Radiation Medicine Chinese Academy of Medical Sciences. The Sprague Dawley rat is an outbred multipurpose breed of albino rat used

extensively in medical research because of its calmness and ease of handling. Thus we used SD rats for pulmonary edema imaging experiment. The protocol was completed in 10 anesthetized male SD rats, comprising 5 in group 1 (control) and 5 in group 2 (oleic acid). Mean body weight and length were, respectively, $310 \pm 6$ g and $14.3 \pm 0.6$ cm in group 1 (control) and $308 \pm 10$ g and $14.5 \pm 0.5$ cm in group 2 (oleic acid).

### 6.2. Anesthesia and Instrumentation

The animals fasted overnight. A 3D rat thoracic model was constructed by performing CT scans on rats. After the rat was successfully anesthetized using a gas anesthesia machine, the rat is placed in a supine position and intubated using an endotracheal tube. The ventilator is set to a positive end-expiratory pressure of 10.7 cmH2O and a tidal volume ($V_T$) of 4 ml/kg for standardized ventilation (Figure 12). The rat received 100% oxygen, and the respiratory rate is maintained at 80 breaths per minute [34, 35].

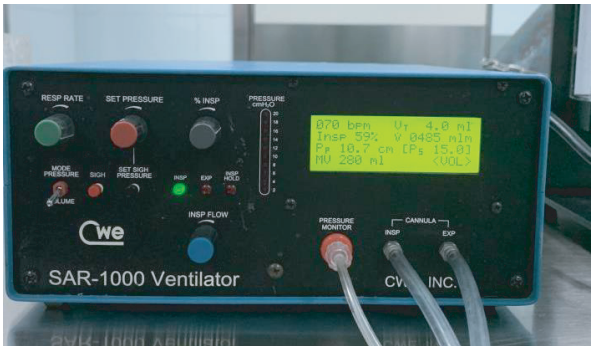


**Figure 12.** Ventilator parameter settings.

Experiments are performed on SD rats using the TGU-EIT system (Figure 13) [36]. The electrodes are 10 mm patch electrodes. After removing the hair around the rat thorax, an average of 16 electrodes of equal size were placed around the rat thorax (Figure 14).

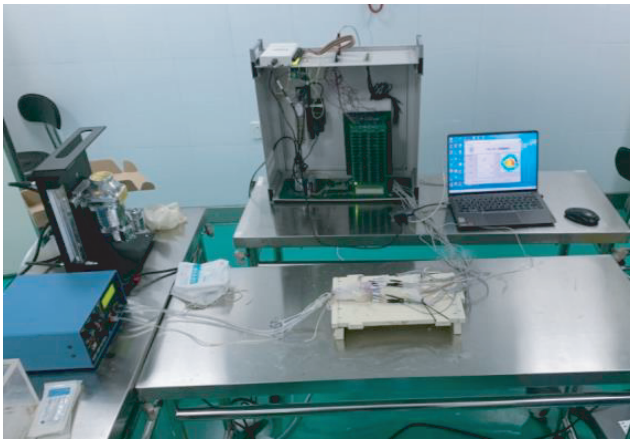

**Figure 13.** TGU-EIT system for rat experiment.

**Figure 14.** Experimental rat and electrodes.

### 6.3. Experimental Protocol

The animals were divided into two experimental groups. The first group (control group) served as a sham group and did not undergo pulmonary edema induction. In the second group (oleic acid group),

pulmonary edema was induced indirectly through the vascular bed by intravenous application of oleic acid. Oleic acid has a direct toxic effect on endothelial cells, leading to epithelial injury characterized by swelling and necrosis formation [37]. As a result, there is a significant increase in pulmonary microvascular permeability, leading to the leakage of protein-rich fluid into the interstitial space [38].

Baseline measurements were conducted on all healthy animals, and measurements were taken on animals positioned at three different locations. To induce gravity-dependent redistribution of pulmonary edema, the animals were rotated transversely along their longitudinal axis to achieve supine position, left tilt of 45 degrees, and right tilt of 45 degrees, respectively.

After baseline measurements, the duration of pulmonary edema persisted for more than 20 minutes. In group 1 (control group), standardized ventilation was continued and no pulmonary edema was induced. In group 2 (oleic acid), the injection of oleic acid was repeated along the tail vein of the rat until a total dose of 0.1 ml/kg was achieved [39]. At the same time, a ventilator was used for standardized ventilation.

After inducing lung injury for 20 minutes, we conducted continuous ventilation measurements on the animals. Upon completing data acquisition, the animals were euthanized immediately during deep anesthesia.

### 6.4. Data Collection

In the adjacent driving mode, a 50 kHz frequency and 5 mA current signal were applied to a pair of adjacent electrodes, and then the differential voltage was measured across the remaining adjacent electrode pairs. For a single cycle of a 16-electrode EIT system, a total of 208 voltage measurements can be obtained when all adjacent electrode pairs are excited [40]. Therefore, a collection of electrodes were used for voltage measurement. The measurement data were collected at a particular moment of end-inspiration. Differential imaging experiments of the whole process of standardized ventilation and pulmonary edema were performed on rat in three defined body positions. 3D-TV algorithm was used to generate 20 EIT images per second for each rat, representing breathing related regional changes of impedance. EIT data acquisition was performed under baseline and injured lung conditions. Image reconstruction and analysis of the collected voltage data were performed at the end of the experiment.

Figure 15 displays the voltage measurement sequences at the end-inspiration status for rats with standardized ventilation and pulmonary edema, respectively. It can be seen that when the rat gets pulmonary edema, the voltage collected by the electrodes is lower than that during standard ventilation.

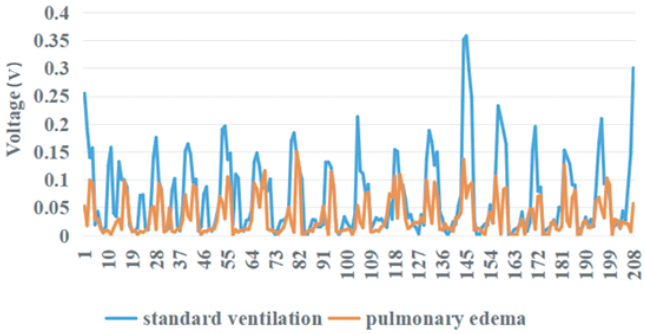


**Figure 15.** Voltage comparison between standard ventilation and pulmonary edema.

### 6.5. Reconstruction Results of the 3D-TV Method

Similar to the simulation, the measurements from the single-ring electrode covered the reconstruction of 45 layers of the entire thorax. Figure 16 compares the CG, TV, and 3D-TV reconstructions of the lung during standardized ventilation for the same rat. It can be seen that compared with the results obtained by other methods, the reconstruction results of the 3D-TV method show good edge preservation effect and ability of artifact removal.

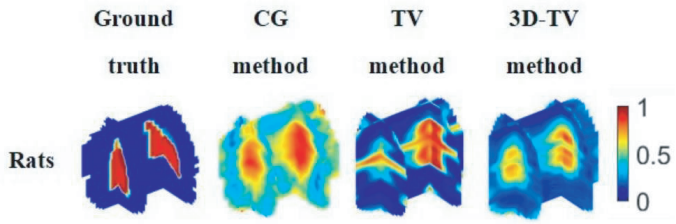


**Figure 16.** 3D lung of rat reconstruction results based on experimental data.

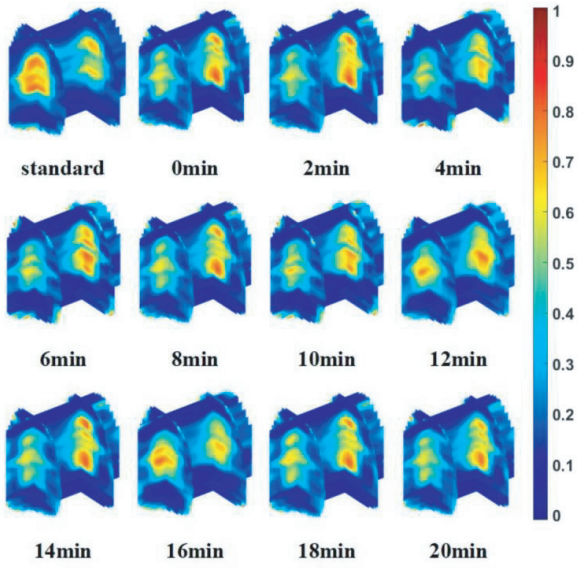


**Figure 17.** 3D reconstruction results at different time points during standardized ventilation in rat.

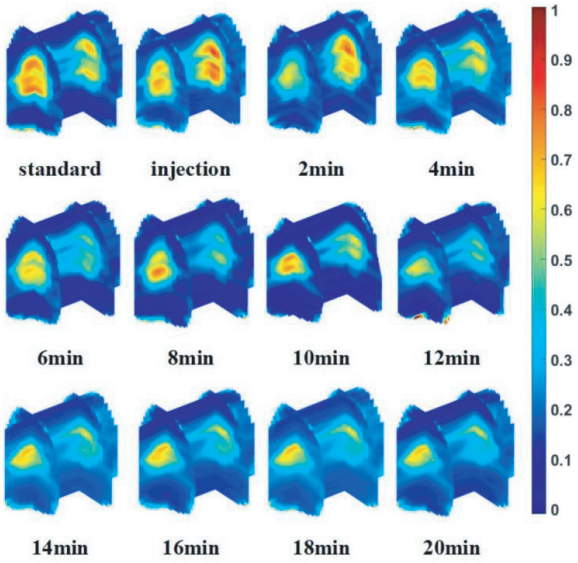


**Figure 18.** 3D reconstruction results at different time points during pulmonary edema in rat.

During the experimental process, we continued to observe the real-time imaging of the lungs in rats with standardized ventilation and pulmonary edema at different time points. Figure 17 illustrates the 3D-TV reconstructions of the lung at different time points during standardized ventilation for the same rat. It can be seen that there is no significant change in the distribution of electrical impedance in the lungs of rats. Figure 18 depicts the 3D-TV reconstructions of the lung at different time points during the progression of pulmonary edema in the control group of rats. It can be seen that within 12 minutes after the injection of oleic acid, the distribution of electrical impedance in the lungs changed significantly, indicating that with the development of pulmonary edema, the water content of the alveoli increased, and the lung damage was aggravated. It can be inferred that the rat lung was significantly edematous.

### 6.6. Data Processing of EIT Data and Calculation of Lung Water $Ratio_{EIT}$

In order to analyze the variation of lung impedance during pulmonary edema, the average impedances of 2D and 3D EIT lung images at different time points during standardized ventilation and pulmonary are calculated. Figure 19 presents the average impedance changes in the lungs of rats undergoing standardized ventilation and pulmonary edema at various time points. It can be seen from Figure 19 that, compared to standard ventilation, the average voltage in rat lungs gradually decreased and eventually stabilized with the development of pulmonary edema, indicating that the average impedance of the rat lung gradually decreased. Once the rat lung became completely edema, the average impedance no longer exhibited any changes.

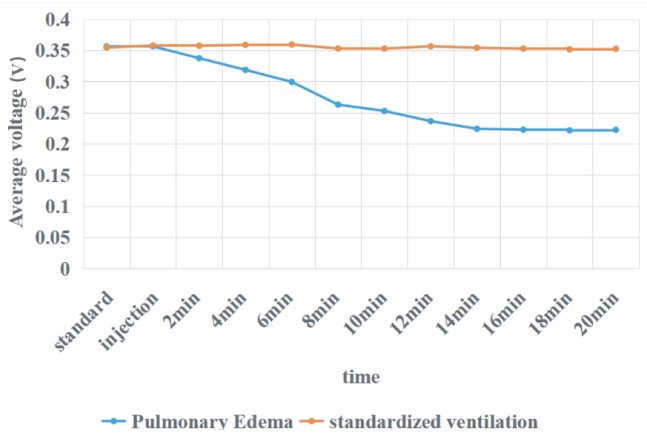


**Figure 19.** Average voltage of the whole rat lung at each time points during standard ventilation and pulmonary edema.

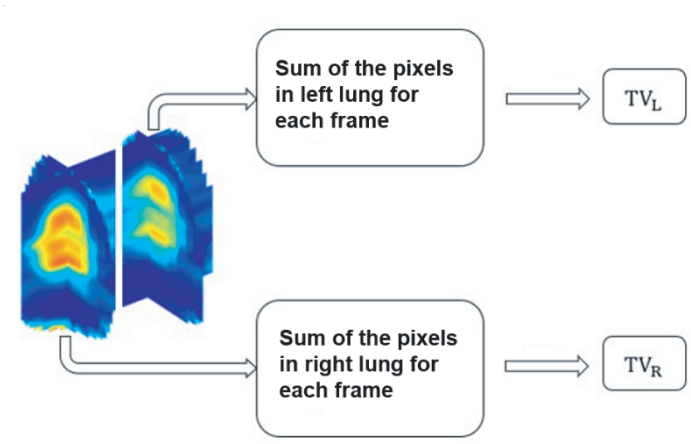


**Figure 20.** Extracting tidal ventilation for the left and right lungs.

Tidal ventilation refers to the ventilation of the lungs that occurs during respiratory processes. The tidal ventilation within the left and the right lungs were calculated as $TV_L$ and $TV_R$ based on the sum of the voxels for each lung separately (Figure 20). By calculating the Imbalance Index $IM_{L-R}$, we can assess the ratio between ventilation in the left and right lungs.

$$IM_{L-R} = \frac{\sqrt{TV_L} - \sqrt{TV_R}}{\sqrt{TV_L} + \sqrt{TV_R}} \tag{18}$$

With the baseline and pulmonary edema conditions, the imbalance coefficient ($IM_{L-R}$) was calculated for each rat at each position, with $+1$ indicating only the left lung is ventilated ($TV_R = 0$) and $-1$ indicating only the right lung is ventilated ($TV_L = 0$).

Body rotation or postural changes can affect the distribution of lung ventilation and pulmonary edema in various ways. We utilized a dataset collected at three different positions (left tilt, horizontal, and right tilt) to calculate the trend line (Figure 21) for standard ventilation and pulmonary edema, assuming a distance of 0.5 on the $x$-axis between two successive positions. The parameter lung water $ratio_{EIT}$ represents the slope of the trend line.

For healthy rats with standard ventilation, only the mechanical properties of air in the lungs need to be considered. However, for rats with pulmonary edema, both the mechanical properties of air and the fluid in the lungs need to be taken into account simultaneously. It can be seen from Figure 21(a)

that the $IM_{L-R}$ of left tilt is positive, indicating that the $TV_L$ is greater than that of the $TV_R$. The $IM_{L-R}$ of right tilt is negative, indicating that the $TV_R$ is greater than that of the $TV_L$, and the lung water $ratio_{EIT}$ of standard ventilation is negative. It can be seen from Figure 21(b) that the $IM_{L-R}$ of left tilt is negative. Since pulmonary edema [41] is mainly distributed in the left lung according to gravity, the $TV_L$ is less than that of the $TV_R$ for left tilt position. The $IM_{L-R}$ of right tilt is positive and due to gravity, pulmonary edema is mainly distributed in the right lung, the $TV_R$ is less than that of the $TV_L$, and the lung water $ratio_{EIT}$ of pulmonary edema is positive. It can be seen that the lung water $ratio_{EIT}$ in rats with pulmonary edema was significantly increased compared with that during standard ventilation, indicating that the content of lung water in the lungs increased.

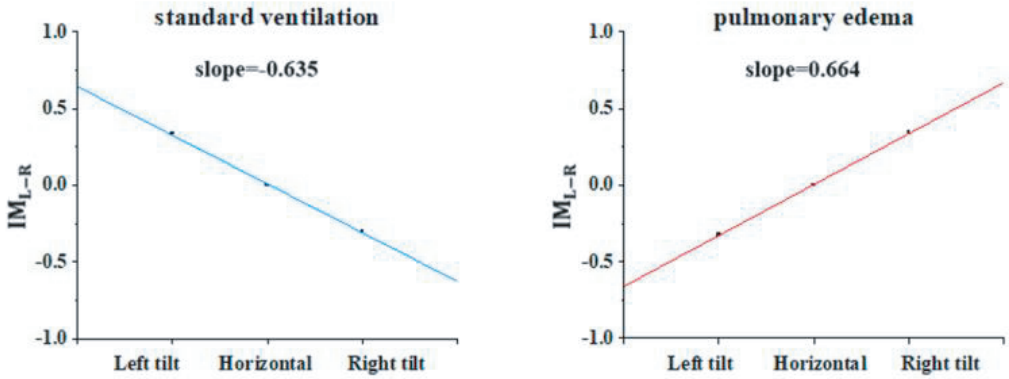


**Figure 21.** Lung water $ratio_{EIT}$. (a) Conditions in standard ventilation. (b) Conditions in pulmonary edema.

## 7. CONCLUSIONS

The Split-Bregman algorithm is used to solve 3D-TV problem for EIT image reconstruction. The rat pulmonary edema experiment was carried out, and the whole process of rat pulmonary edema was monitored through 3D EIT in real time. The experimental results show that 3D EIT could give more information for the preoperative and postoperative lung conditions of patients in clinical practice compared with traditional medical imaging techniques, e.g., CT.

In future work, 3D EIT images will be reconstructed under the framework of compressed sensing to improve the real-time performance of dynamic EIT reconstruction. Considering the complexity of 3D modeling, it is feasible to preestablish thoracic models based on standard anatomical configurations for both forward and inverse calculations in clinical applications. The development of a multi-layer electrode 3D EIT system would be advantageous as it facilitates 3D reconstruction and regional lung ventilation monitoring. Further research will also encompass 3D modeling incorporating geometric changes during the respiratory and cardiac cycles to ensure comprehensive information capture.

## ACKNOWLEDGMENT

The authors would like to acknowledge the support of this research from the National Natural Science Foundation of China (Grants No. 61872269, No. 61903273, No. 62072335 and No. 62071328) and to thank the Open project of Medical and Industrial Integration Laboratory in the Affiliated Jiangning Hospital of Nanjing Medical University (JNYYZXKY202104).

## REFERENCES

1. Murray, J. F., "Pulmonary edema: Pathophysiology and diagnosis," *International Journal of Tuberculosis and Lung Disease*, Vol. 15, No. 2, 155–160, 2011.

2. Schwaiberger, D., P. A. Pickerodt, A. Pomprapa, O. Tjarks, F. Kork, W. Boemke, et al., "Closed-loop mechanical ventilation for lung injury: A novel physiological-feedback mode following the principles of the open lung concept," *Journal of Clinical Monitoring and Computing*, Vol. 32, No. 3, 493–502, 2018.
3. Bodenstein, M., M. David, and K. Markstaller, "Principles of electrical impedance tomography and its clinical application," *Critical Care Medicine*, Vol. 37, No. 2, 713–724, 2009.
4. Tingay, D. G., M. J. Wallace, R. Bhatia, G. M. Schmolzer, V. A. Zahra, M. J. Dolan, et al., "Surfactant before the first inflation at birth improves spatial distribution of ventilation and reduces lung injury in preterm lambs," *Journal of Applied Physiology*, Vol. 116, No. 3, 251–8, 2014.
5. Herrero, R., G. Sanchez, and J. A. Lorente, "New insights into the mechanisms of pulmonary edema in acute lung injury," *Annals of Translational Medicine*, Vol. 6, No. 2, 32, 2018.
6. Park, S., R. Farah, S. M. Shea, E. Tryggestad, R. Hales, and J. Lee, "Simultaneous tumor and surrogate motion tracking with dynamic MRI for radiation therapy planning," *Physics in Medicine and Biology*, Vol. 63, No. 2, 025015, 2018.
7. Balachandran, R., D. Schurzig, J. M. Fitzpatrick, and R. F. Labadie, "Evaluation of portable CT scanners for otologic image-guided surgery," *International Journal of Computer Assisted Radiology and Surgery*, Vol. 7, No. 2, 315–321, 2012.
8. Schullcke, B., S. Krueger-Ziolek, B. Gong, R. A. Jorres, U. Mueller-Lisse, and K. Moeller, "Ventilation inhomogeneity in obstructive lung diseases measured by electrical impedance tomography: A simulation study," *Journal of Clinical Monitoring and Computing*, Vol. 32, No. 4, 753–761, 2018.
9. Crabb, M. G., J. L. Davidson, R. Little, P. Wright, A. R. Morgan, C. A. Miller, et al., "Mutual information as a measure of image quality for 3D dynamic lung imaging with EIT," *Physiological Measurement*, Vol. 35, No. 5, 863–879, 2014.
10. Fan, W. and H. X. Wang, "3D modelling of the human thorax for ventilation distribution measured through electrical impedance tomography," *Measurement Science and Technology*, Vol. 21, No. 11, 115801-1–8, 2010.
11. Frerichs, I., "Electrical impedance tomography (EIT) in applications related to lung and ventilation: A review of experimental and clinical activities," *Physiological Measurement*, Vol. 21, No. 2, R1–R21, 2000.
12. Adler, A., M. B. Amato, J. H. Arnold, R. Bayford, M. Bodenstein, S. H. Bohm, et al., "Whither lung EIT: Where are we, where do we want to go and what do we need to get there?," *Physiological Measurement*, Vol. 33, No. 5, 679–694, 2012.
13. Javaherian, A., M. Soleimani, and K. Moeller, "A fast time-difference inverse solver for 3D EIT with application to lung imaging," *Medical & Biological Engineering & Computing*, Vol. 54, No. 8, 1243–55, 2016.
14. Martin, S. and C. T. M. Choi, "A post-processing method for three-dimensional electrical impedance tomography," *Scientific Reports*, Vol. 7, 7212, 2017.
15. Dimas, C., N. Uzunoglu, and P. P. Sotiriadis, "An efficient point-matching method-of-moments for 2D and 3D electrical impedance tomography using radial basis functions," *IEEE Transactions on Biomedical Engineering*, Vol. 69, No. 2, 783–794, 2022.
16. Sun, B. Y., S. H. Yue, Z. H. Hao, Z. Q. Cui, and H. X. Wang, "An improved Tikhonov regularization method for lung cancer monitoring using electrical impedance tomography," *IEEE Sensors Journal*, Vol. 19, No. 8, 3049–3057, 2019.
17. Tawil, D. S., D. Rye, and M. Velonaki, "Improved image reconstruction for an EIT-based sensitive skin with multiple internal electrodes," *IEEE Transactions on Robotics*, Vol. 27, No. 3, 425–435, 2011.
18. Gong, B., B. Schullcke, S. Krueger-Ziolek, F. Zhang, U. Mueller-Lisse, and K. Moeller, "Higher order total variation regularization for EIT reconstruction," *Medical & Biological Engineering & Computing*, Vol. 56, No. 8, 1367–1378, 2018.

19. Borsic, A. and A. Adler, "A primal-dual interior-point framework for using the L1 or L2 norm on the data and regularization terms of inverse problems," *Inverse Problems*, Vol. 28, No. 9, 095011, 2012.
20. Brito-Loeza, C., R. Legarda-Saenz, and A. Martin-Gonzalez, "A fast algorithm for a total variation based phase demodulation model," *Numerical Methods for Partial Differential Equations*, Vol. 36, No. 3, 617–636, 2020.
21. Strauss, T. and T. Khan, "Statistical inversion in electrical impedance tomography using mixed total variation and non-convex $l(p)$ regularization prior," *Journal of Inverse and Ill-Posed Problems*, Vol. 23, No. 5, 529–542, 2015.
22. Gonzalez, G., V. Kolehmainen, and A. Seppanen, "Isotropic and anisotropic total variation regularization in electrical impedance tomography," *Computers & Mathematics with Applications*, Vol. 74, No. 3, 564–576, 2017.
23. Tehrani, J. N., A. McEwan, C. Jin, and A. van Schaik, "L1 regularization method in electrical impedance tomography by using the L1-curve (Pareto frontier curve)," *Applied Mathematical Modelling*, Vol. 36, No. 3, 1095–1105, 2012.
24. Wu, C. Y., Z. H. Wei, H. Bi, B. C. Zhang, Y. Lin, and W. Hong, "InSAR imaging based on L1 regularisation joint reconstruction via complex approximated message passing," *Electronics Letters*, Vol. 54, No. 4, 237–239, 2018.
25. Mamatjan, Y., A. Borsic, D. Gursoy, and A. Adler, "An experimental clinical evaluation of EIT imaging with $l(1)$ data and image norms," *Physiological Measurement*, Vol. 34, No. 9, 1027–1039, 2013.
26. Liu, J. Z., L. Lin, W. B. Zhang, and G. Li, "A novel combined regularization algorithm of total variation and Tikhonov regularization for open electrical impedance tomography," *Physiological Measurement*, Vol. 34, No. 7, 823–838, 2013.
27. Borsic, A., B. M. Graham, A. Adler, and W. R. B. Lionheart, "In vivo impedance imaging with total variation regularization," *IEEE Transactions on Medical Imaging*, Vol. 29, No. 1, 44–54, 2010.
28. de Munck, J. C., T. J. C. Faes, and R. M. Heethaar, "The boundary element method in the forward and inverse problem of electrical impedance tomography," *IEEE Transactions on Biomedical Engineering*, Vol. 47, No. 6, 792–800, 2000.
29. Abascal, J., J. Chamorro-Servent, J. Aguirre, S. Arridge, T. Correia, J. Ripoll, et al., "Fluorescence diffuse optical tomography using the split Bregman method," *Medical Physics*, Vol. 38, No. 11, 6275–6284, 2011.
30. Yang, J. F., Y. Zhang, and W. T. Yin, "A fast alternating direction method for TVL1-L2 signal reconstruction from partial fourier data," *IEEE Journal of Selected Topics in Signal Processing*, Vol. 4, No. 2, 288–297, 2010.
31. Yang, J. F. and Y. Zhang, "Alternating direction algorithms for $l(1)$-problems in compressive sensing," *Siam Journal on Scientific Computing*, Vol. 33, No. 1, 250–278, 2011.
32. Xu, W. H., Y. N. Xie, X. Zhang, and W. Li, "Cerebral angiography under artificial intelligence algorithm in the design of nursing cooperation plan for intracranial aneurysm patients in craniotomy clipping," *Computational and Mathematical Methods in Medicine*, 2182931, 2022.
33. Wang, Q., J. M. Wang, X. Y. Li, X. J. Duan, R. H. Zhang, H. Zhang, et al., "Exploring respiratory motion tracking through electrical impedance tomography," *IEEE Transactions on Instrumentation and Measurement*, Vol. 70, 1–12, 2021.
34. Gao, X. W., P. Y. Qian, D. Cen, W. J. Hong, Q. Peng, and M. Xue, "Synthesis of phosphatidylcholine in rats with oleic acid-induced pulmonary edema and effect of exogenous pulmonary surfactant on its De Novo synthesis," *Plos One*, Vol. 13, No. 3, 1–13, 2018.
35. Gomez-Laberge, C., J. H. Arnold, and G. K. Wolf, "A unified approach for EIT imaging of regional overdistension and atelectasis in acute lung injury," *IEEE Transactions on Medical Imaging*, Vol. 31, No. 3, 834–42, 2012.
36. Li, X. Y., X. J. Chen, Q. Wang, J. M. Wang, X. J. Duan, Y. K. Sun, et al., "Electrical-impedance-tomography imaging based on a new three-dimensional thorax model for assessing the extent of lung injury," *Aip Advances*, Vol. 9, No. 12, 125310, 2019.

37. Trepte, C. J. C., C. R. Phillips, J. Sola, A. Adler, S. A. Haas, M. Rapin, et al., "Electrical impedance tomography (EIT) for quantification of pulmonary edema in acute lung injury," *Critical Care*, Vol. 20, 18, 2016.
38. Riera, J., P. J. Riu, P. Casan, and J. R. Masclans, "Electrical impedance tomography in acute lung injury," *Medicina Intensiva*, Vol. 35, No. 8, 509–517, 2011.
39. Hagawane, T. N., R. V. Gaikwad, and N. A. Kshirsagar, "Dual hit lipopolysaccharide & oleic acid combination induced rat model of acute lung injury/acute respiratory distress syndrome," *Indian Journal of Medical Research*, Vol. 143, 624–632, 2016.
40. Wang, Q., H. Y. Zhang, X. Y. Li, X. J. Duan, J. M. Wang, R. H. Zhang, et al., "Error-constraint deep learning scheme for electrical impedance tomography (EIT)," *IEEE Transactions on Instrumentation and Measurement*, Vol. 71, 1–11, 2022.
41. Quintel, M., P. Pelosi, P. Caironi, J. P. Meinhardt, T. Luecke, P. Herrmann, et al., "An increase of abdominal pressure increases pulmonary edema in oleic acid-induced lung injury," *American Journal of Respiratory and Critical Care Medicine*, Vol. 169, No. 4, 534–541, 2004.